ACS APPLIED MATERIALS & INTERFACES

Article

Morphological Evolution of Multilayer Ni/NiO Thin Film Electrodes during Lithiation

Guennadi Evmenenko, Timothy T. Fister, D. Bruce Buchholz, Qianqian Li, Kan-Sheng Chen, Jinsong Wu, Vinayak P. Dravid, Mark C Hersam, Paul Fenter, and Michael J. Bedzyk

ACS Appl. Mater. Interfaces, **Just Accepted Manuscript** • DOI: 10.1021/acsami.6b05040 • Publication Date (Web): 15 Jul 2016

ACS Publications

ACS Applied Materials & Interfaces is published by the American Chemical Society. 1155 Sixteenth Street N.W., Washington, DC 20036

Morphological Evolution of Multilayer Ni/NiO Thin Film Electrodes during Lithiation

Guennadi Evmenenko,[†] Timothy T. Fister,[‡] D. Bruce Buchholz,[†] Qianqian Li,[#] Kan-Sheng Chen,[†] Jinsong Wu,[†,#] Vinayak P. Dravid,[†] Mark C. Hersam,[†,&] Paul Fenter,[‡] Michael J. Bedzyk[†]

[†]*Department of Materials Science and Engineering, Northwestern University, Evanston, Illinois 60208, United States*

[‡]*Chemical Sciences and Engineering Division, Argonne National Laboratory, Lemont, Illinois 60439, United States*

[#]EPIC, NUANCE Center, Northwestern University, *Evanston, Illinois 60208, United States*

[&]*Department of Chemistry, Northwestern University, Evanston, Illinois 60208, United States*

*E-mail: bedzyk@northwestern.edu

ABSTRACT: Oxide conversion reactions in lithium ion batteries are challenged by substantial irreversibility associated with significant volume change during the phase separation of an oxide into lithia and metal species (e.g., $NiO + 2Li^+ + 2e^- \rightarrow Ni + Li_2O$). We demonstrate that the confinement of nanometer-scale NiO layers within a Ni/NiO multilayer electrode can direct lithium transport and reactivity, leading to coherent expansion of the multilayer. The morphological changes accompanying lithiation were tracked in real-time by *in-operando* X-ray reflectivity (XRR) and *ex-situ* cross-sectional transmission electron microscopy on well-defined periodic Ni/NiO multilayers grown by pulsed-laser deposition. Comparison of pristine and lithiated structures reveals that the nm-thick nickel layers help initiate the conversion process at the interface and then provide an architecture that confines the lithiation to the individual oxide layers. XRR data reveal that the lithiation process starts at the top and progressed through the electrode stack, layer by layer resulting in a purely vertical expansion. Longer term cycling showed significant reversible capacity (~800 mA h g^{-1} after ~100 cycles), which we attribute to a combination of the intrinsic bulk lithiation capacity of the NiO and additional interfacial lithiation capacity. These observations provide new insight into the role of metal/metal oxide

interfaces in controlling lithium ion conversion reactions by defining the relationships between morphological changes and film architecture during reaction.

KEYWORDS: *lithium-ion battery, nickel oxide, conversion reaction, multilayer thin-film electrodes*

INTRODUCTION

Nanostructured materials hold the key to fundamental advances in energy conversion and storage.[1-3] Interfacial space-charge effects at the nanoscale can result in substantial improvement of properties. Consequently, extensive research is underway on nanostructured thin film electrodes with various electrochemical reaction mechanisms based on nanometer-size effects, chemical composition and structure.[4-19]

There have been several attempts to improve the electrochemical performance of thin films electrodes for rechargeable lithium-ion batteries (LIBs) by introducing a secondary material layer that is used to alleviate the volumetric change in the electrode and prevent the aggregation of the active materials. For lithium ion anode materials, an effective implementation of this concept is to use a multilayer thin film structure compromised of Si (or other high capacity materials) and inert metal layers (e.g., Ti, Al, Zn). Recent studies of Si-based multilayer electrodes show strong differences in reversible capacity and cycling stability as a function of the thicknesses of the buffer and active layers.[5-17]

The technical challenges of Li-alloying reactions (e.g., with Si) are similar to those found in the conversion reactions of metal oxide electrodes. First demonstrated by Tarascon et al., the lithiation of NiO follows a displacement process with the reversible formation of Li_2O accompanied by the reduction of the transition metal leading to Ni nanoparticles in the range of 10-100 Å in diameter.[20] In particular, the electrochemically driven confinement of nano-sized metal particles is believed to enhance their electrochemical reactivity towards the formation/decomposition of Li_2O. [20-22] In order to explore the critical role of nanoscale confinement and the role of the interfaces in controlling these reactions, we use our previously demonstrated approach[12] of multilayer electrodes that consist of alternating layers of active and inactive materials (e.g., NiO and Ni layers, respectively) grown on flat substrates. In particular, NiO, a prototypical Li-ion conversion material is a conceptually promising electrode material for LIBs due to abundance, low cost, and high theoretical specific capacity (718 mA h g^{-1}). However, the implementation of NiO and other conversion electrode in LIBs is greatly hindered by a number of factors, including its poor long-term cycling stability and rate performance due to the significant dimensional and volume changes during electrochemical cycling deformations and degradation of the electrode, including fragmentation, disintegration, fracturing, and loss in contact between current collectors and the active electrode materials.[23] A second significant issue

is the substantial overpotentials[24] that are observed with conversion materials that are associated with the nucleation of metal nanoparticles within a Li_2O matrix.

Multilayer electrodes have the benefits of: 1) controlled nm-thick electrodes that can benefit from nanoscale confinement while having substantially larger total active layer thicknesses than a single thin film, and 2) enhancing the role of the interface between active and inactive materials. Previous X-ray reflectivity (XRR) results confirmed the ability of multilayer architectures to substantially enhance structural reversibility during lithium insertion and extraction for Si and CrO_x active layers under potentiostatic control.[19] Ultimately, this digitized vertical architecture provides the potential to combine the fast kinetics of nanostructured electrodes with improved reversibility and significantly higher capacities.

For this study our multilayer is synthesized as a periodic set of Ni/NiO bilayers with individual active layer thicknesses ranging from 20-100 Å. We use a combination of *in-operando* synchrotron X-ray reflectivity along with *ex-situ* transmission electron microscopy (TEM) to monitor the structural and morphological changes in NiO-based multilayer electrodes as a function of applied potential during the first lithiation reaction to obtain an improved molecular-based understanding of the processes that controls the performance of these conversions reaction. The lithiation reaction leads to the phase separation of Ni nanoparticles dispersed within a Li_2O matrix, although the interstitial metal layers confine these species. We also observe that the Ni-layer thickness increases upon lithiation, indicating that the interface is, in fact, an active component in the reaction. Real-time measurements reveal the lithiation proceeds vertically, layer by layer through the electrode. This structural mechanism is complemented by extended cycling data that demonstrates how controlling nanoscale electrode morphology can be a powerful design approach for improving the reversibility of conversion material electrodes.

EXPERIMENTAL SECTION

The nickel metal / nickel oxide multilayer films were grown by pulsed-laser deposition (PLD) on 10x3x1 mm sapphire α-Al_2O_3 (1-102) substrates (CrysTec GmbH, Germany). The sample was fully immersed in a 'transmission-geometry' X-ray compatible electrochemical cell[8] such that the scattering plane aligned to the shorter 3 mm dimension, which called for the substrates to be cut 3-mm wide along the glancing incident X-ray beam direction and 10-mm wide transverse to the beam. Separate Ni and NiO PLD targets were used to grow 5 Ni/NiO bilayers with the

thickness of each layer controlled by adjusting the number of laser pulses. The heterostructure was masked from the bottom nickel layer, providing 3 mm tabs for electrical contact from top spring electrodes.

The *in-operando* XRR experiments were performed at the Advanced Photon Source (APS) at photon energies of E = 20.00 keV and 17.50 keV. The X-ray beam size was collimated to 1.0x0.25 mm^2 and the scattered X-ray intensity was acquired with a Pilatus 100k detector. Full reflectivity data sets were measured in 15 min and were collected repeatedly during electrochemical cycling. The samples were contained in an X-ray compatible electrochemical cell with a lithium metal counter/reference electrode[8] and fully immersed in a 1 M solution of $LiPF_6$ or $LiClO_4$ in 1:1 ratio of ethylene carbonate and dimethyl carbonate by volume.

XRR analysis used Motofit[25] with a multiple-slab model that included a sapphire substrate, 5 Ni/NiO bilayers, and an electrolyte. Structural parameters for sapphire and the electrolyte were fixed, whereas the parameters for the buffer and active layers (electron density, interface roughness, and layer thickness) were allowed to vary. The electron densities were initially estimated based on the chemical composition of the multilayer electrode components. Table S1 lists calculated electron densities of bulk materials relevant to this study. For lithiated samples the structural model included variable electron densities and thicknesses of active NiO-based layers and variable Ni-layer thicknesses with an electron density that was fixed to a value obtained from the analysis of the pristine as-deposited samples. In some cases, the fits made use of a parameter that nominally varies the energy resolution of the X-ray beam. In this case, this parameter is used as a phenomenological approach to incorporate the heterogeneity of the multilayer structure (e.g., the layer spacing)

The lithiated and partially lithiated thin film cross-sectional samples were prepared using a focused ion beam (FIB) system (FEI Helios Nanolab 600 DualBeam FIB/SEM). A JEOL-2100F transmission electron microscope (TEM) at 200 kV was used to characterize the films by both high-resolution electron microscopy (HREM) and Z-contrast STEM with a high angle annular dark-field detector. X-ray energy dispersive spectra (EDS) and electron energy loss spectra were collected with the JEOL-2100F.

RESULTS AND DISCUSSION

In-operando XRR measurements of the structural changes in Ni/NiO multilayer films during the first discharge (i.e. lithiation) of a half-cell consisting of the film and a lithium metal reference electrode were performed under potentiostatic control starting at the open circuit condition (3.0 V). During the cycle, the potential was swept at a rate of 2 mV/s with potential holds at 0.1-0.5 V intervals. XRR scans were repeated at all intermediate voltages until an equilibrium structure was established as evidenced by no further changes in the XRR pattern. For the *in-operando* experiment, a 5-bilayer film with nominal 20 Å thicknesses for buffer Ni layers and 50 Å for the active layers of NiO was chosen. Figure 1 shows the sequence of XRR patterns measured for this multilayer film during lithiation. To emphasize changes the reflectivity data, $R(q)$, is normalized to the reflectivity from a single interface by being multiplied by q^4, where $q = (4\pi/\lambda)\sin\theta$ is X-ray momentum transfer along the surface normal. The corresponding Patterson functions, $P(z)$, shown in Figure 2 are obtained by taking the Fourier transform of the Fresnel-normalized reflectivity data $R(q)/R_F(q)$.[26-28] These directly indicate the presence of electron density fluctuations in the films without any model assumptions or fitting procedures. The positions of the peaks in $P(z)$ correspond to the distances between interfaces where the electron density changes. As seen in Figures 1 and 2, Li-ion insertion causes major structural reorganization within the multilayer film as indicated by distinctive changes to the XRR patterns and Patterson functions, which were drastically modified starting at 0.6 V.

At the open circuit condition (3.0 V) (pristine film), the XRR data reveals a complex 5-bilayer structure for the film. The XRR pattern (top of Figure 1) exhibits prominent Bragg peaks due to the repeated bilayer spacing that confirms the rather high degree of order for this multilayer vertical architecture. As expected for N = 5 periods, there are N-2 subsidiary peaks (or Kiessig interference fringes) between the Bragg peaks. The Patterson function (top of Figure 2) at this initial open circuit condition shows a large primary maximum at 380 Å corresponding to the overall film thickness, and secondary peaks at positions corresponding to Ni/NiO interface

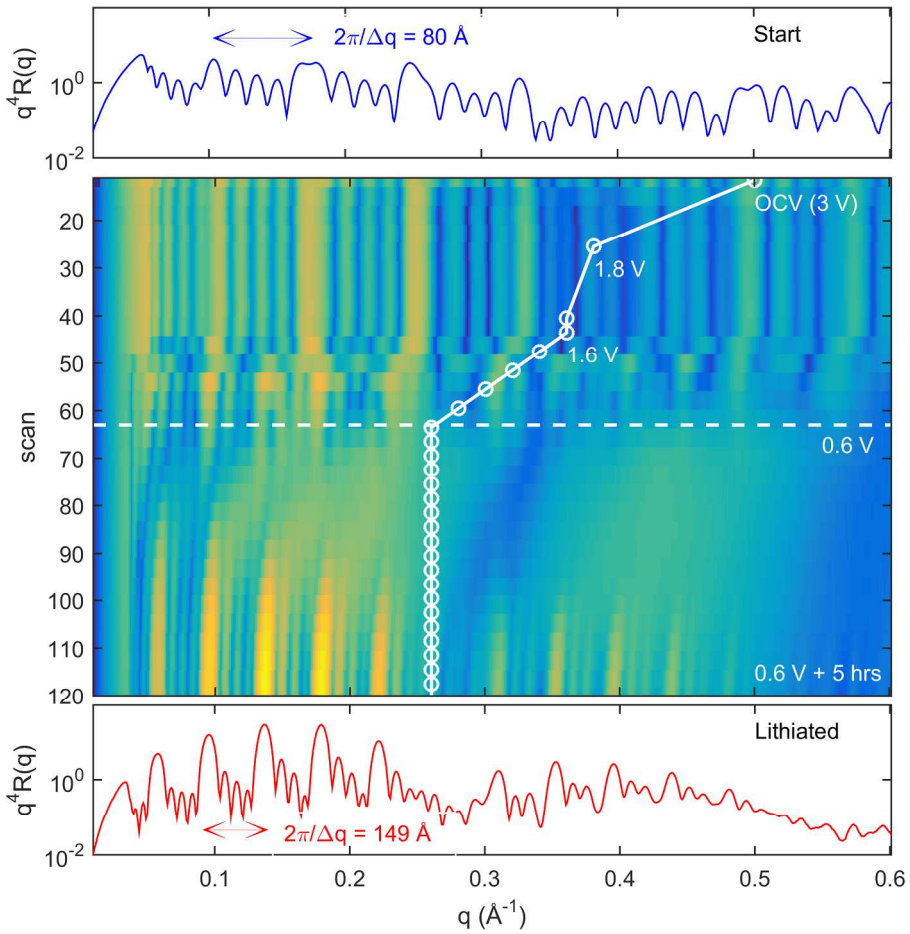

Figure 1. *In operando* normalized XRR data collected during the first discharge (lithiation). The top panel shows the first XRR scan. The bottom shows the last scan. The middle panel shows scans 1 through 120 along with the set voltage at the time of the scan (white open circles).

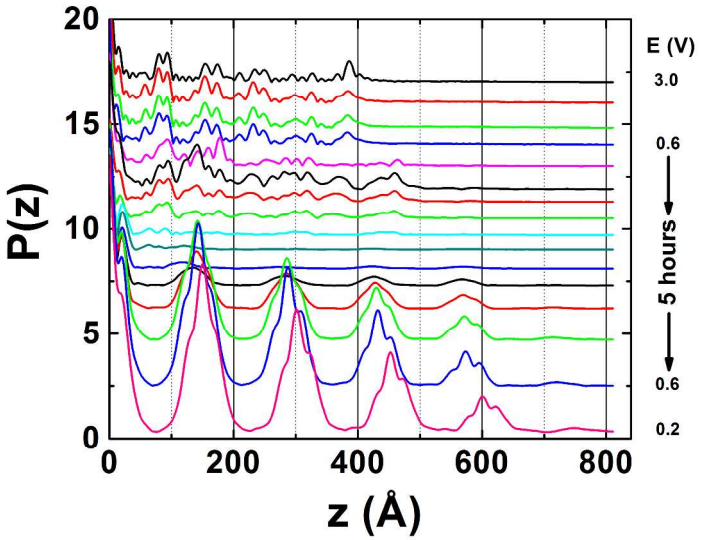

Figure 2. Patterson functions derived from the XRR data shown in Figure 1. The curves are shifted vertically for clarity.

separation distances consistent with the expected thicknesses of 20 Å (Ni) and 50 Å (NiO) in the as-grown multilayer film. Temporal changes in reflectivity patterns and the corresponding Patterson functions are seen to be small until the potential reaches 0.6 V, where the abrupt onset of lithiation occurred. The flattening of Kiessig fringes (associated with the overall thickness of the film) and Bragg peaks from the film bilayer structure in the beginning of insertion of lithium ions transforms to an appearance of new Bragg peaks, which correspond to an increased *d*-spacing of 140 Å consistent with the conversion of the bilayer to Ni/Li_2O. Kiessig fringes grow prominently during the potential hold at 0.6 V suggesting that the surface becomes smoother and more laterally uniform. The increase in Bragg peak intensity and the height of the Patterson function also confirms that the bilayer *d*-spacing becomes highly uniform, indicating a constant state of lithiation throughout the multilayer after 5 hours (this will be discussed in detail later). A further evidence of drastic morphological changes in Ni/NiO multilayer film during lithium ion insertion can be seen in Figure 3, where XRR data are presented for the region near the critical angles for total external reflection from the sapphire substrate and the film. (A list of the critical momentum transfer values $q_c \propto \sqrt{\rho_e - \rho_e^{electrolyte}}$ calculated from the modeled electron

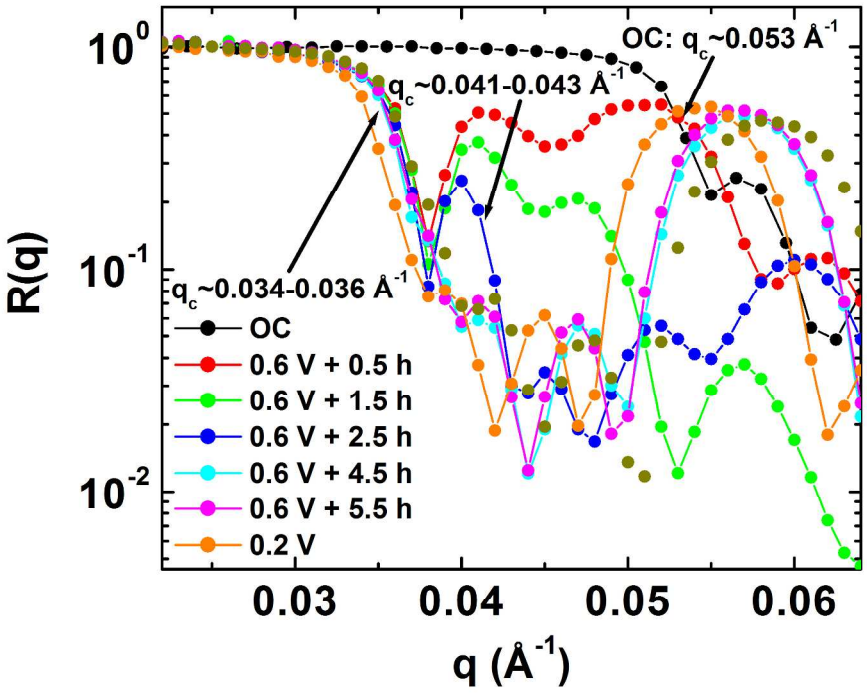

Figure 3. XRR data in the region of total reflection for the Ni/NiO multilayer film at various stages of lithiation.

densities (ρ_e) for the components of the lithiated Ni/NiO multilayer film can be found in Table S1.) The q_c values can be expected to shift from 0.053 $Å^{-1}$ (corresponding to the average electron density of the pristine 5-bilayer Ni/NiO film), to an intermediate value of 0.041-0.043 $Å^{-1}$ (during major lithium ion insertion) to a lower value for the sapphire substrate in contact with the electrolyte of 0.034-0.036 $Å^{-1}$ (most appropriate for the last stage of lithiation). At the end of lithium insertion, the structural adjustment to the equilibrium morphology with stoichiometric ratio between Ni and Li_2O takes place. Abrupt changes to the critical angle just after lithiation begins and the coexistence of different critical angles, which correspond to different components or states of the multilayer electrode (sapphire, partially and fully lithiated film, pristine film), indicate that the observed structural changes exhibit non-uniform character in both the normal and lateral directions.

Starting with the model dependent XRR data analysis for the structurally stable morphologies of Ni/NiO multilayer film, the specular X-ray reflectivity data (solid circles) and best fits (solid lines) are shown for the pristine film and fully lithiated 5-bilayer Ni/NiO film (at 0.6 V) in Figure 4. The corresponding electron density profiles determined from the best fits are presented in Figure 5. The pristine film consists of five bilayers of Ni and NiO with slightly varied thicknesses of individual layers: 16-18 Å for Ni and 58-62 Å for NiO, with an overall thickness of ~377 Å and surface roughness of 5.2 Å (these values are close to the expected thicknesses from the PLD process). The experimentally obtained electron densities 2.59 $e^-Å^{-3}$ (for Ni) and 2.04 $e^-Å^{-3}$ (for NiO) are in agreement with calculated bulk values of 2.60 $e^-Å^{-3}$ and 1.97 $e^-Å^{-3}$, respectively. (See Table S1.) The overall thickness of the fully lithiated multilayer film increased to 740 Å (approximately twice the original thickness) accompanied by a lowering of the electron density of the active layers to 1.1 $e^-Å^{-3}$ corresponding to a film of Ni nanoparticles within a Li_2O matrix. This is close to the calculated value of 1.20 $e^-Å^{-3}$, which corresponds to the stoichiometric composition of Ni and Li_2O after NiO is fully lithiated as a result of the conversion reaction. The top layer of the multilayer film has a 10% lower density, which most probably corresponds to a slightly greater fraction of Li_2O in this outermost layer.

The XRR data analysis indicates a uniform electron density profile within each oxide layer, implying that the reduced Ni nanoparticles are randomly distributed within the Li_2O matrix

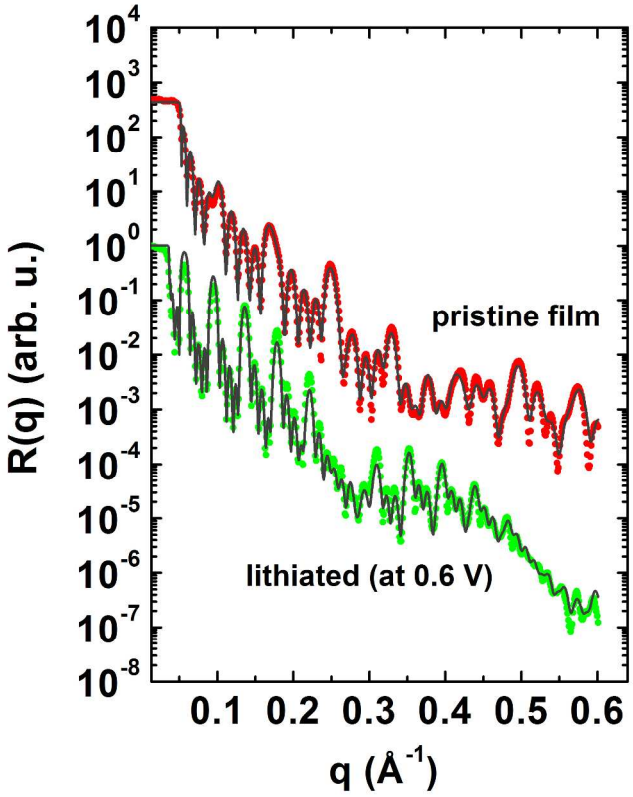

Figure 4. The specular XRR data (solid circles) and best fits (solid lines) for a 5-bilayer Ni/NiO film: pristine film (red) and fully lithiated film at 0.6 V (green). The experimental and theoretical curves are shifted vertically for clarity.

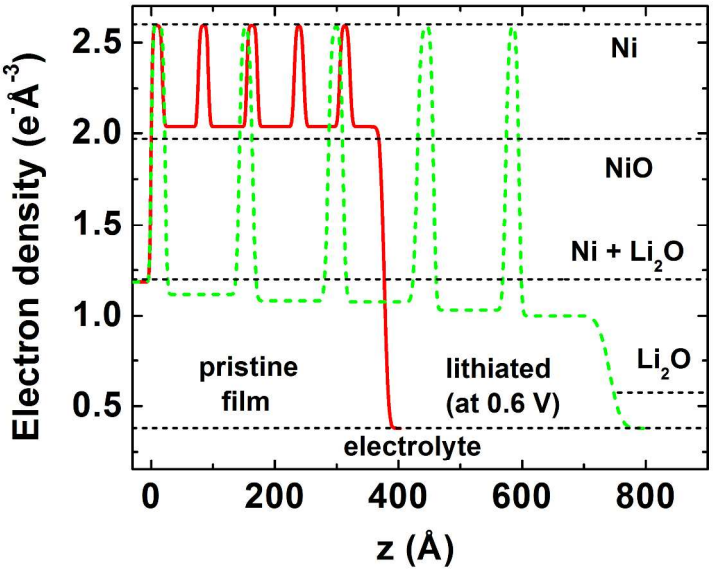

Figure 5. Electron density profiles obtained from best fits of the XRR data shown in Fig. 3 (solid red line: pristine film and dashed green line: lithiated film). Calculated electron densities for the electrolyte, Ni, NiO, Li_2O and expected electron density of the fully lithiated NiO layer (Ni+Li_2O) are shown by dotted lines for comparison.

without locally expressed variation both within each layer and between different layers of the multilayer film. Analysis of the electron density profiles shown in Figure 5 reveals an increased thickness of each buffer Ni layer by 6-7 Å for the lithiated sample as compared to the pristine as-grown multilayer. This effect can be explained as nucleation and growth of reduced Ni on both sides of the original Ni layers. In comparison, the bulk crystal (111) atomic layer spacing of Ni is 2.0 Å, suggesting that the amount of Ni that nucleated at the Ni-NiO interface from the lithiating NiO layer consisted of 1-2 atomic layers of Ni[29] (corresponding up to 10% of the total Ni in the NiO film). Moreover, the shifting of the broad lobes of scattering (near q = 0.2 and 0.4 Å^{-1} in Figure 1) shows that the Ni layer thickness begins to increase well before the reappearance of Bragg peaks due to periodic multilayer structure. This suggests that the interfacial nucleation precedes the 3D (random) nucleation of nickel in each oxide layer.

Our next question is related to the structural changes observed in Figures 1 and 2 for the individual layers of the multilayer during the first 2.5 hours of lithiation. These observations are complicated by structural changes due to kinetic effects occurring during the 15 minutes of XRR data collection for each scan. Moreover, such analysis is also hampered by lateral inhomogeneities within the multilayer. Despite these problems, we were able to produce reasonable fits to some of the experimental XRR data for the early stages of lithium-ion insertion. Figure S1 shows the XRR data and best fits, and Figure 6 shows the corresponding electron density profiles for the multilayer at 0.5 and 2.5 hours after the voltage was set to 0.6 V (where the abrupt onset of lithiation occurred). Electron density profiles for the pristine film and for the fully lithiated film are shown for comparison. For the 0.5 and 2.5 hour cases, lateral non-uniformity was considered as a major factor that smeared out the distinctive features of the XRR

data (Kiessig fringes and Bragg peaks) and was accounted for by increasing the uncertainty in *q* during fitting procedure (see Figure S1). It is interesting to see from Figure 6, that lithium insertion and the related conversion reaction starts at the top layers of the multilayer film and diffuses inward as time progresses. After 0.5 hours at 0.6 V, the electron density of the three top active layers drops to a value nearly equivalent to the electron density of all active layers after 2.5 h and 5.0 h (fully lithiated film). The density changes are accompanied by twofold expansion of these layers that leads to an increasing of the overall thickness of the film from 377 Å to 575 Å. The thicknesses of the adjusted Ni layers increase by 6.6 Å on average. After 0.5 hrs at 0.6 V, the structural parameters of the two bottom active and buffer layers remain practically unchanged. These layers begin to lithiate after 2.5 hours and the overall film thickness

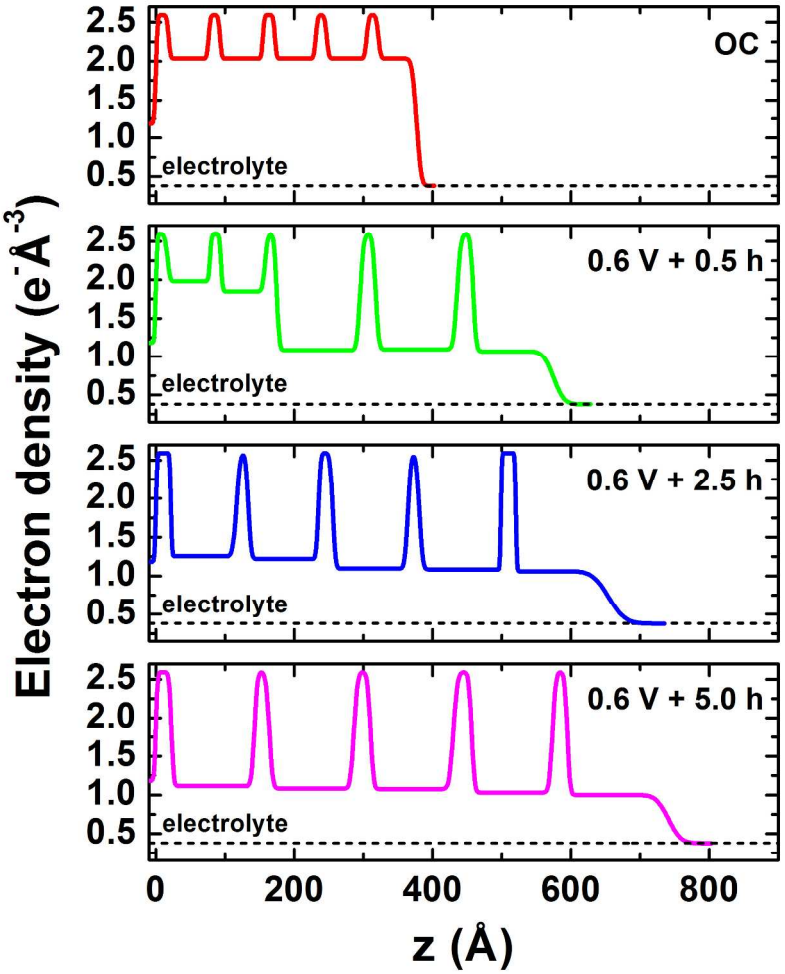

Figure 6. XRR determined electron density profiles for 5-bilayer Ni/NiO film during Li-ion insertion at early stage of lithiation. Electron density profile for the fully lithiated film (at 0.6 V + 5.5 h) is shown for comparison.

reaches ~655 Å after 2.5 hours, but complete lithiation, coinciding with the new multilayer Bragg peaks, requires five hours.

Such a mechanism for lithium ion incorporation also adequately explains the changes observed in Figure 3 for the XRR region near the critical angles of the film and substrate; namely different and multiple critical angles occurring at intermediate stages of lithiation and the existence of one critical angle for the fully lithiated film. It should be noted that a simple calculation of the average electron density from Fig. 6 of the fully lithiated film is ~1.20 $e^{-}Å^{-3}$. This corresponds to $q_{c,exp}$ = 0.034 $e^{-}Å^{-3}$, which coincidently matches that for the sapphire substrate (see Table S1).

After 2.5 h at 0.6 V (i.e., near scan number 96), we observe distinctive changes in XRR patterns with a growth of the characteristic diffraction features in the XRR data (Figures 1 and 2). Figure S2 represents the XRR data (solid circles) and best fits (solid lines) during the last 1.5 hours of lithiation at 0.6 V. As can be seen, the positions of the Bragg peaks remain practically fixed in q for all XRR patterns, whereas the peak intensities grow until the lithiated film reaches its equilibrium state at this potential. Such structural behavior can be explained by the opposite process to smearing of XRR patterns due to increasing of non-uniformity that was observed during early stage of lithiation. We have obtained good fits of the presented XRR curves when relative uncertainty of X-ray momentum transfer was varied from 5% to 1.5% as the lithiated film became laterally uniform. The corresponding electron density profiles are presented in Figure 7. Some changes of

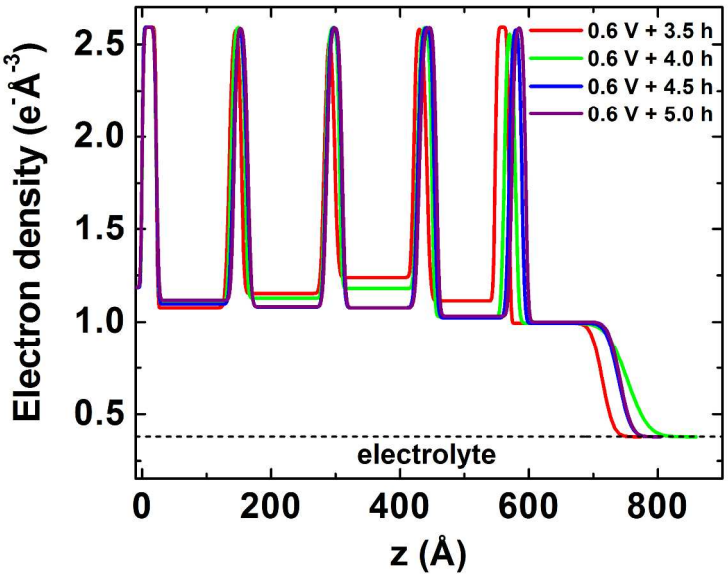

Figure 7. Electron density profiles of a 5-bilayer Ni/NiO film for the latter stages of lithiation.

the electron density profiles can be interpreted in terms of slight adjustments in coherency between bilayers of the lithiated multilayer film in the vertical direction and strong increases in their lateral uniformity, especially within the top active layers. Such a structural recovery of multilayer digital topology occurring after film expansion during the last hour of lithiation can be explained by a confinement effect in thin active layers of the multilayer structure. The ultrathin morphology of the digitized architecture of Ni/NiO multilayer film affects the electrochemical processes in different active layers of this film during lithium-ion insertion that results in anisotropic structural rearrangement at the intermediate stage of lithiation and requires additional time for structural adjustment to the equilibrium state during the final stage. Analysis of the Fig. 7 XRR data shows a slight decrease in the electron density (by 5-10%) of the lithiated active layers that can be interpreted in terms of additional accumulation of lithium ions inside the Li_2O volume. Larger changes to electron density of top layer were observed to support our conclusion.

Similar structural changes were observed for Ni/NiO multilayer films with thicker NiO active layers. The specular X-ray reflectivity patterns and the corresponding Patterson functions are shown in Figures S3 and S4 for 5-bilayer Ni/NiO film with ~10 Å of Ni and 105 Å NiO layers before and after complete lithiation. This fully lithiated sample with double expansion was used for *ex-situ* cross-sectional transmission electron microscopy. The TEM images for the pristine and fully lithiated samples are shown in Figures S5 and 8. These images confirm the general

results found by XRR data, namely the two-fold expansion of each oxide layer during lithiation and the confinement of these active regions between the nanometer-thick Ni interlayers.

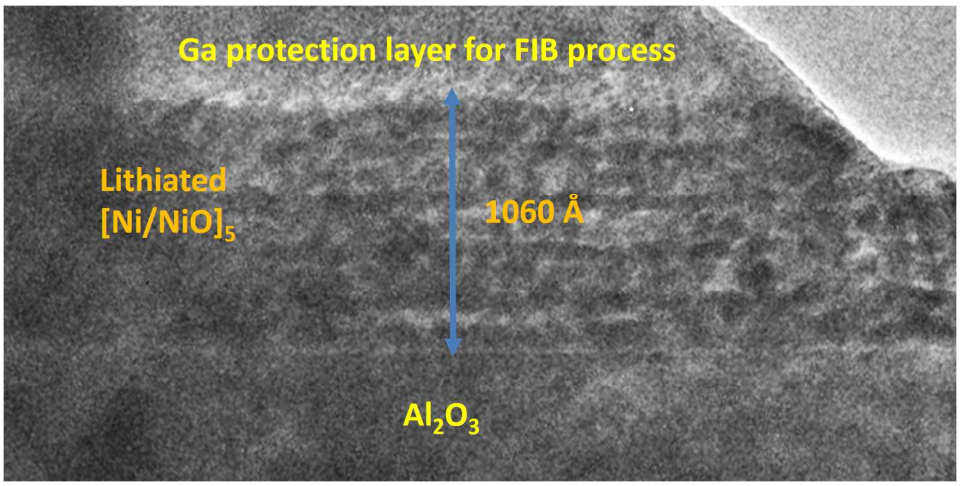

Figure 8. Cross-sectional TEM image of the lithiated 5-bilayer Ni/NiO (10 Å / 105 Å) film (the darker contrast represents heavier elements).

The electron nano-beam diffraction patterns (Figures 9 and S6) reveal clear Ni diffraction rings and weak rings for nanocrystalline Li_2O. No rings appear that can be indexed as NiO; consistent with the full lithiation and conversion of the NiO layers in this multilayer film. These results suggest that discrete Ni and Li_2O particles form within each layer, and the TEM images (especially the high-resolution image in Figure S5B) reveal some non-uniformity of density at length-scales up to 100 Å within the lithiated active layers. This non-uniformity was not observable by specular XRR

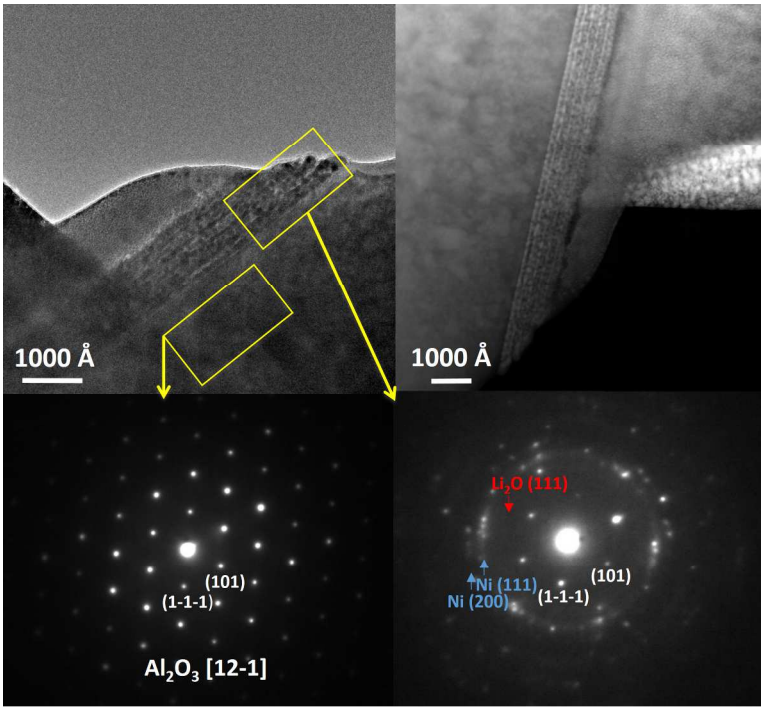

Figure 9. Nano-beam electron diffraction patterns of the lithiated 5-bilayer Ni/NiO (10 Å / 105 Å) film.

analysis, but should be observable with future off-specular grazing incidence small angle scattering experiments.

To examine the effect of morphology on the electrochemical performance of the Ni/NiO multilayer film as an electrode, charge/discharge cycling tests were conducted on a single bilayer Ni/NiO (20 Å / 250 Å) film and 5-bilayer (20 Å / 50 Å) film grown directly on Cu foils by pulsed laser deposition. Coin cells were fabricated using Li metal as the counter electrode, Celgard 2320 as the separator, and 1M $LiPF_6$ in 1:1 (v/v) EC/DMC as the electrolyte. The specific capacities of the Ni/NiO bilayer and 5-bilayer electrodes measured at a 0.5 C current rate and within a voltage window of 0.1 V to 2.4 V are shown in Figure 10. The values of the specific capacities are both normalized based on the mass of NiO layers only. The first cycle charge capacities in both cases are about 1500 mA h g^{-1}, which is twice the theoretical value for NiO (718 mA h g^{-1}). After the batteries are cycled for about 50 cycles, the capacities for both cases become stabilized and plateau at the value of 820 mA h g^{-1}. The specific capacity of NiO being higher than the theoretical value has been reported previously[30-35] and has been attributed to the reversible formation and deformation of a solid electrolyte interface (SEI).[33-34] More interestingly, the specific capacities for both cases after reaching the plateau at 100th cycle

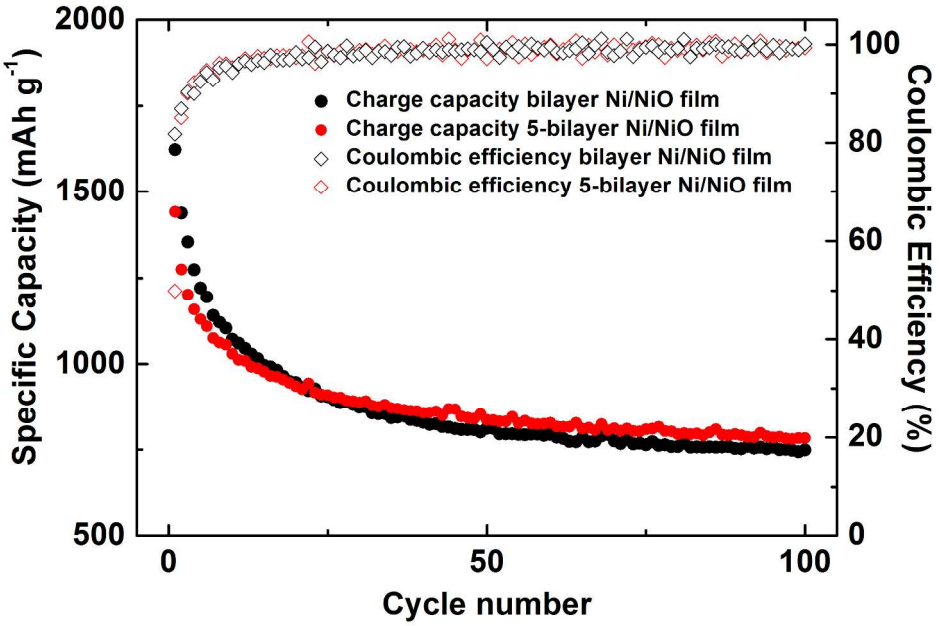

Figure 10. Specific capacities and coulombic efficiency of the coin cell batteries made by bilayer Ni/NiO (20 Å / 250 Å) and 5-bilayer Ni/NiO (20 Å / 50 Å) films and Li metal as counter electrodes.

remain higher than the theoretical value, indicating the fact that the reversible side reactions do not completely vanish even after prolonged electrochemical cycling. Comparing the bilayer Ni/NiO electrodes to the multilayer ones, the electrochemical performances are very similar.

CONCLUSIONS

Real-time *in-operando* synchrotron XRR and *ex-situ* cross-sectional TEM have been used to characterize the morphological changes in 5-bilayer Ni/NiO sandwich-like thin films as electrode materials for lithium-ion batteries during lithiation. Analysis of the XRR data shows that the lithiation process of multilayer Ni/NiO electrodes start at the top layers and then progresses vertically toward the bottom of the stack. The observed structural changes have been accompanied with volume expansion of lithiated active layers and development of the lateral non-uniformity within the multilayer structure that was distinctively indicated by smearing out of Kiessig fringes and Bragg peaks in XRR patterns. We believe that the ultrathin topology of the multilayer structure promotes fast anisotropic Li-ion insertion inside the film that leads to expected film expansion but this process is accompanied by development of lateral non-uniformity. When lithium-ion insertion reaches its limit, volume of the lithiated NiO layers has increased to twice the original value for the pristine films. Thereafter, the structural modification

resulting in improvement of lateral uniformity of the lithiated multilayer architecture and its coherent adjustment is observed that resulted in distinctive enhancement of the characteristic features (Kiessig fringes and Bragg peaks) of the XRR patterns during the last stage of lithiation. This structural rearrangement without noticeable changes in overall film thickness can be attributed to effect of confinement conditions of ultrathin active layers in the vertically digitized multilayer structure of Ni/NiO electrodes. The XRR does not show any electron density fluctuation inside the fully lithiated active layers of the multilayer film within the limits of experimental accuracy that attests that the reduced Ni is rather uniformly distributed inside the Li_2O matrix after the completion of the conversion reaction. In addition, one or two atomic layers of reduced Ni are accumulated at the surfaces of the Ni buffer layers. This results in XRR measured increased thicknesses of 6-7 Å for all Ni interlayers of the fully lithiated multilayer film.

Our in-operando structural studies of vertically digitized multilayer electrodes were designed to allow one to establish relationships between the morphological changes and the film architecture during lithiation. We analyzed the mechanisms of the observed structural transformations and discovered the process of incorporation of lithium ions into ultrathin multilayer films during the first discharge of the NiO-based electrodes. This work will thus inform ongoing efforts to understand and improve the performance of oxide conversion reactions in lithium ion batteries.

ACKNOWLEDGMENTS

This research was supported by the Center for Electrochemical Energy Science, an Energy Frontier Research Center funded by the U.S. Department of Energy, Office of Science, Office of Basic Energy Sciences, under Contract No. DE-AC02-06CH11357. We thank the beamline staff at 33BM and DND-CAT, Advanced Photon Source (APS), which provided valuable assistance. DND-CAT is supported by E. I. duPont de Nemours & Co., Northwestern University, Dow Chemical Co., the State of Illinois through the Department of Commerce and the Board of Education (HECA), and the US National Science Foundation. We acknowledge the use of Northwestern facilities including the NUANCE Center and X-ray Diffraction Facility that are supported by the MRSEC through NSF Contract No. DMR-1121262.

Supporting Information Available

Details of multilayer film growth; tabulated mass density, calculated electron density, and critical momentum transfer values of assumed components of the Ni/NiO multilayer electrode; the parameters used in the profiles obtained by the best fits of X-ray reflectivity (XRR) data; XRR data for a 5-bilayer Ni/NiO film during Li-ion insertion at the early and the later stages of lithiation; XRR data and the corresponding Patterson functions for pristine and lithiated 5-bilayer Ni/NiO (10 Å / 105 Å) film; high resolution cross-sectional TEM images of the pristine and the lithiated 5-bilayer Ni/NiO (10 Å / 105 Å) film near the sapphire substrate. This material is available free of charge via the Internet at http://pubs.acs.org.

REFERENCES

(1) Aricò, A. S.; Bruce, P.; Scrosati, B.; Tarascon, J. M.; Van Schalkwijk, W. Nanostructured Materials for Advanced Energy Conversion and Storage Devices. *Nat. Mater.* **2005,** *4* (5), 366-377.

(2) Etacheri, V.; Marom, R.; Elazari, R.; Salitra, G.; Aurbach, D. Challenges in the Development of Advanced Li-Ion Batteries: a Review. *Energy Environ. Sci.* **2011,** *4* (9), 3243-3262.

(3) Nitta, N.; Wu, F. X.; Lee, J. T.; Yushin, G. Li-Ion Battery Materials: Present and Future. *Mater. Today* **2015,** *18* (5), 252-264.

(4) Zhou, Y. N.; Xue, M. Z.; Fu, Z. W. Nanostructured Thin Film Electrodes for Lithium Storage and All-Solid-State Thin-Film Lithium Batteries. *J. Power Sources* **2013,** *234*, 310-332.

(5) Goriparti, S.; Miele, E.; Angelis, F. D.; Fabrizio, E. D.; Zaccaria, R. P.; Capiglia, C. Review on Recent Progress of Nanostructured Anode Materials for Li-Ion Batteries. *J. Power Sources* **2014,** *257*, 421-443.

(6) Kim, J. B.; Lee, H. Y.; Lee, K. S.; Lim, S. H.; Lee, S. M. Fe/Si Multi-Layer Thin Film Anodes for Lithium Rechargeable Thin Film Batteries. *Electrochem. Commun.* **2003,** *5* (7), 544-548.

(7) Kim, J. B.; Jun, B. S.; Lee, S. M. Improvement of Capacity and Cyclability of Fe/Si Multilayer Thin Film Anodes for Lithium Rechargeable Batteries. *Electrochim. Acta* **2005,** *50* (16-17), 3390-3394.

(8) Fister, T. T.; Long, B. R.; Gewirth, A. A.; Shi, B.; Assoufid, L.; Lee, S. S.; Fenter, P. Real-Time Observations of Interfacial Lithiation in a Metal Silicide Thin Film. *J. Phys. Chem.* **2012,** *116*, 22341-22345.

(9) Li, H. X.; Bai, H. M.; Tao, Z. L.; Chen, J. Si-Y Multi-Layer Thin Films as Anode Materials of High-Capacity Lithium-Ion Batteries. *J. Power Sources* **2012,** *217*, 102-107.

(10) Kang, H. K.; Lee, S. R.; Cho, W. I.; Cho, B. W. Effect of Multilayer Structure on Cyclic Performance of Si/Fe Anode Electrode in Lithium-Ion Secondary Batteries. *Phys. Chem. Chem. Phys.* **2013,** *15* (5), 1569-1577.

(11) Wang, J.; Tong, Y. F.; Xu, Z.; Li, W. H.; Yan, P. X.; Chung, Y. W. Amorphous Silicon/Carbon Multilayer Thin Films as the Anode for High Rate Rechargeable Li-Ion Batteries. *Mater. Lett.* **2013,** *97*, 37-39.

(12) Fister, T. T.; Esbenshade, J.; Chen, X.; Long, B. R.; Shi, B.; Schleputz, C. M.; Gewirth, A. A.; Bedzyk, M. J.; Fenter, P. Lithium Intercalation Behavior in Multilayer Silicon Electrodes. *Adv. Energy Mater.* **2014,** *4*, 1301494 (6).

(13) Tong, Y. F.; Xu, Z.; Liu, C.; Zhang, G. A.; Wang, J.; Wu, Z. G. Magnetic Sputtered Amorphous Si/C Multilayer Thin Films as Anode Materials for Lithium Ion Batteries. *J. Power Sources* **2014,** *247*, 78-83.

(14) Pang, C. L.; Li, N.; Wang, C. X. Intercalated SiO_2&Si/Carbon Composite for High Capacity Li Ion Battery Anodes. *Electrochim. Acta* **2014,** *141*, 226-233.

(15) Demirkan, M. T.; Trahey, L.; Karabacak, T. Cycling Performance of Density Modulated Multilayer Silicon Thin Film Anodes in Li-Ion Batteries. *J. Power Sources* **2015,** *273*, 52-61.

(16) Mori, T.; Chen, C. J.; Hung, T. F.; Mohamed, S. G.; Lin, Y. Q.; Lin, H. Z.; Sung, J. C.; Hu, S. F.; Liu, R. S. High Specific Capacity Retention of Graphene/Silicon Nanosized Sandwich Structure Fabricated by Continuous Electron Beam Evaporation as Anode for Lithium-Ion Batteries. *Electrochim. Acta* **2015,** *165*, 166-172.

(17) Ashuri, M.; He, Q. R.; Shaw, L. L. Silicon as a Potential Anode Material for Li-Ion Batteries: Where Size, Geometry and Structure Matter. *Nanoscale* **2016,** *8* (1), 74-103.

(18) Roy, P.; Srivastava, S. K. Nanostructured Anode Materials for Lithium Ion Batteries. *J. Mater. Chem. A* **2015,** *3* (6), 2454-2484.

(19) Fister, T. T.; Hu, X. Y.; Esbenshade, J.; Chen, X.; Wu, J. S.; Dravid, V.; Bedzyk, M.; Long, B.; Gewirth, A. A.; Shi, B.; Schleputz, C. M.; Fenter, P. Dimensionally Controlled Lithiation of Chromium Oxide. *Chem. Mater.* **2016,** *28* (1), 47-54.

(20) Poizot, P.; Laruelle, S.; Grugeon, S.; Dupont, L.; Tarascon, J. M. Nano-Sized Transition-Metaloxides as Negative-Electrode Materials for Lithium-Ion Batteries. *Nature* **2000,** *407* (6803), 496-499.

(21) Laruelle, S.; Grugeon, S.; Poizot, P.; Dollé, M.; Dupont, L.; Tarascon, J. M. On the Origin of the Extra Electrochemical Capacity Displayed by MO/Li Cells at Low Potential. *J. Electrochem. Soc.* **2002,** *149* (5), A627-A634.

(22) Wang, G. X.; Chen, Y.; Konstantinov, K.; Lindsay, M.; Liu, H. K.; Dou, S. X. Investigation of Cobalt Oxides as Anode Materials for Li-Ion Batteries. *J. Power Sources* **2002,** *109* (1), 142-147.

(23) Mukhopadhyay, A.; Sheldon, B. W. Deformation and Stress in Electrode Materials for Li-Ion Batteries. *Prog. Mater. Sci.* **2014,** *63*, 58-116.

(24) Cabana, J.; Monconduit, L.; Larcher, D.; Palacín, M. R.,Beyond Intercalation-Based Li-Ion Batteries: the State of the Art and Challenges of Electrode Materials Reacting through Conversion Reactions. *Adv. Mater.* **2010,** *22* (35), E170-E192.

(25) Nelson, A., Co-Refinement of Multiple-Contrast Neutron/X-Ray Reflectivity Data using MOTOFIT. *J. Appl. Crystallogr.* **2006,** *39*, 273-276.

(26) Tolan, M., *X-ray scattering from soft-matter thin film: materials science and basic research*. Springer-Verlag: Berlin, 1999; Vol. 148, p. 197.

(27) Evmenenko, G.; Stripe, B.; Dutta, P. Morphological Behavior of Thin Polyhedral Oligomeric Silsesquioxane Films at the Molecular Scale. *J. Colloid Interface Sci.* **2011,** *360* (2), 793-799.

(28) It should be noted that we have used $(q^2 - q_c^2)^{1/2}$ instead of q so as to include refraction inside the film (see Table S1).

(29) Slater, J. C. Atomic Radii in Crystals. *J. Chem. Phys.* **1964,** *41* (10), 3199-3204.

(30) Zou, Y. Q.; Wang, Y. NiO Nanosheets Grown on Graphene Nanosheets as Superior Anode Materials for Li-Ion Batteries. *Nanoscale* **2011,** *3* (6), 2615-2620.

(31) Chen, Z.; Xiao, A.; Chen, Y.; Zuo, C.; Zhou, S.; Li, L. Template-Directed Preparation of Two-Layer Porous NiO Film via Hydrothermal Synthesis for Lithium Ion Batteries. *Mater. Res. Bull.* **2012,** *47* (8), 1987-1990.

(32) Huang, Y.; Huang, X. L.; Lian, J. S.; Xu, D.; Wang, L. M.; Zhang, X. B. Self-Assembly of Ultrathin Porous NiO Nanosheets/Graphene Hierarchical Structure for High-Capacity and High-Rate Lithium Storage. *J. Mater. Chem.* **2012,** *22* (7), 2844-2847.

(33) Caballero, A.; Hernan, L.; Morales, J.; Gonzalez, Z.; Sanchez-Herencia, A. J.; Ferrari, B. A High-Capacity Anode for Lithium Batteries Consisting of Mesoporous NiO Nanoplatelets. *Energy Fuels* **2013,** *27* (9), 5545-5551.

(34) Cao, L.; Wang, D. X.; Wang, R. NiO Thin Films Grown Directly on Cu Foils by Pulsed Laser Deposition as Anode Materials for Lithium Ion Batteries. *Mater. Lett.* **2014,** *132*, 357-360.

(35) Lin, F.; Nordlund, D.; Weng, T. C.; Zhu, Y.; Ban, C. M.; Richards, R. M.; Xin, H. L. Phase Evolution for Conversion Reaction Electrodes in Lithium-Ion Batteries. *Nat. Commun.* **2014,** *5*, 3358

TOC Figure

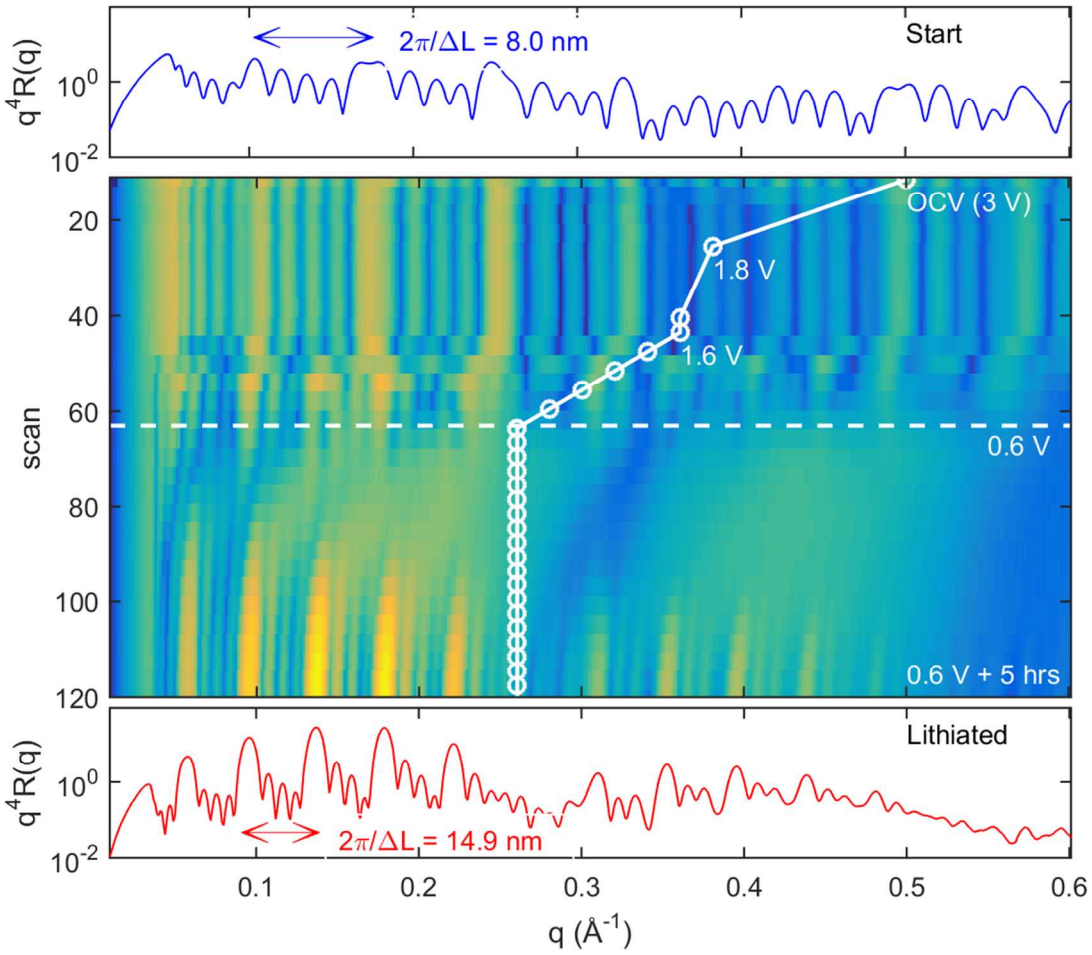
Start
2π/ΔL = 8.0 nm
q⁴R(q)
10⁰
10⁻²
OCV (3 V)
1.8 V
1.6 V
0.6 V
scan
20
40
60
80
100
120
0.6 V + 5 hrs
Lithiated
2π/ΔL = 14.9 nm
0.1
0.2
0.3
0.4
0.5
0.6
q (Å⁻¹)